1 # Enhanced pore space analysis by use of μ-CT, MIP,

2 # NMR, and SIP

4 Zeyu Zhang [1], Sabine Kruschwitz [2, 3], Andreas Weller [4], Matthias Halisch [5]

6 [1] Southwest Petroleum University, School of Geoscience and Technology, 610500 Chengdu, China

7 [2] Federal Institute for Material Research and Testing (BAM), D-12205 Berlin, Germany

8 [3] Technische Universität Berlin, Institute of Civil Engineering, D-13355 Berlin, Germany

9 [4] Clausthal University of Technology, Institute of Geophysics, D-38678 Clausthal-Zellerfeld, Germany

10 [5] Leibniz Institute for Applied Geophysics (LIAG), D-30655 Hannover, Germany

11 *Correspondence to*: Zeyu Zhang (zeyuzhangchina@163.com)

24

25

26

27

28

29

30

31

32

33   **Abstract**

34   We investigate the pore space of rock samples with respect to different petrophysical parameters using

35   various methods, which provide data upon pore size distributions, including micro computed tomography

36   (µ-CT), mercury intrusion porosimetry (MIP), nuclear magnetic resonance (NMR), and spectral induced

37   polarization (SIP). The resulting cumulative distributions of pore volume as a function of pore size are

38   compared. Considering that the methods differ with regard to their limits of resolution, a multiple length

39   scale characterization of the pore space geometry is proposed, that is based on a combination of the results

40   from all of these methods. The approach is demonstrated using samples of Bentheimer and Röttbacher

41   sandstone. Additionally, we compare the potential of SIP to provide a pore size distribution with other

42   commonly used methods (MIP, NMR). The limits of resolution of SIP depend on the usable frequency

43   range (between 0.002 Hz and 100 Hz). The methods with similar resolution show a similar behavior of the

44   cumulative pore volume distribution in the overlapping pore size range. We assume that µ-CT and NMR

45   provide the pore body size while MIP and SIP characterize the pore throat size. Our study shows that a

46   good agreement between the pore radii distributions can only be achieved if the curves are adjusted

47   considering the resolution and pore volume in the relevant range of pore radii. The MIP curve with the

48   widest range in resolution should be used as reference.

49

50   Keywords: Pore Space Analysis, Joint Methods, Fractal Dimension, Spectral Induced Polarization

51   **1 Introduction**

52   Transport and storage properties of reservoir rocks are determined by the size and arrangement of the pores.

53   Different methods have been developed to determine the pore size distribution of rocks. These methods are

54   based on different physical principles. Therefore, it can be expected that the methods recognize different

55   geometries and sizes. Additionally, the ranges of pore sizes that are resolved by the methods are different

56   (Meyer et al., 1997). Rouquerol et al. (1994) reported that no experimental method provides the absolute

57   value of parameters such as porosity, pore size, surface area, and surface roughness.

58   Our study of pore space analysis is based on the following methods: micro computed tomography (µ-CT),

59   mercury intrusion porosimetry (MIP), nuclear magnetic resonance (NMR), and spectral induced

60   polarization (SIP). The first three methods can be regarded as standard methods to derive a pore size

61   distribution. The use of SIP in this field has been reported only recently (Revil et al., 2014; Zhang et al.,

62   2017).

63   We are aware that further methods can be applied for the characterization of pore size distribution, e.g.

64   synchrotron-radiation-based computed tomography (Peth et al., 2008), focused ion beam tomography

65   (Keller et al., 2011), transmission electron microscopy (Gaboreau et al., 2012), scanning electron

66 microscopy (SEM), ^{14}C labeled methylmethacrylate method (Kelokaski et al., 2005), and gas adsorption

67 and desorption method (BET) (Avnir and Jaroniec, 1989).

68 A variety of studies has been performed to compare the pore size distribution resulting from different

69 experiments. For example, Mesquita et al. (2016) matched NMR T_2 distributions and capillary pressure

70 curves of carbonate samples using a coupled dual porosity model to estimate the surface relaxivity. Daigle

71 and Johnson (2016) applied percolation theory to determine the pore size distributions combining NMR

72 and capillary pressure measurement. Zhang and Weller (2014) investigated the fractal behavior of the pore

73 volume distribution by capillary pressure curves and NMR T_2 distributions of sandstones. Considering the

74 differences in fractal dimension resulting from the two methods, they concluded a differentiation into

75 surface dimension and volume dimension.

76 An enhanced pore space analysis using different methods should be able to provide a better description of

77 the pore space geometry over a wide range of pore sizes. Our study presents an approach to describe and

78 quantify the pore space geometry of porous material by combining the results of methods with different

79 resolution. Samples of Bentheimer and Röttbacher sandstone are investigated by μ-CT, MIP, NMR, and

80 SIP. The resulting pore size distributions are connected to each other to get two different pore radii

81 distributions, one for the pore body radius and one for the pore throat radius. The comparison of the two

82 curves enables the determination of the ratio between pore body and pore throat radius. Finally, the fractal

83 dimension of the pore volume distribution is determined for the two samples.

84 **2 Methodology**

85 The pore size distribution resulting from different methods has to be compared and evaluated. We prefer a

86 comparison based on the cumulative volume fraction of pores V_c, which is expressed by

87
$$V_c = \frac{V(<r)}{V_p},$$
(1)

88 with V_p being the total pore volume, and $V(<r)$ the cumulative volume of pores with radii less than r. A

89 graph displaying the logarithm of V_c versus the logarithm of the pore radius offers the advantage that the

90 slope of the curves is related to the fractal dimension of the pore volume (Zhang and Weller, 2014).

91 Fractal theory is applied to describe the structure of geometric objects (Mandelbrot, 1977, 1983). At

92 molecular size and microscopic range, surfaces of most materials including those of natural rocks show

93 irregularities and defects that appear to be self-similar upon variation of resolution (Avnir et. al, 1984). A

94 self-similar object is characterized by similar structures at different scales. The regularity of self-similar

95 structures can be quantified by the parameter of fractal dimension D. Pape et al. (1982) first proposed a

96 fractal model (the so called 'pigeon-hole model' or 'Clausthal Concept') for the geometry of rock pores.

97 Fractal dimension describes the size of geometric objects as a function of resolution. This parameter has

98   proved to be useful in the comparison of different methods that determine distributions of geometric objects

99   (e.g. Zhang and Weller, 2014, Ding et al., 2017).

100   The experimental methods used in this study include digital image analysis based upon micro computed

101   tomography (μ-CT), mercury intrusion porosimetry (MIP), nuclear magnetic resonance (NMR), and

102   spectral induced polarization (SIP).

103   The μ-CT method can only resolve the part of the pore space with pore sizes larger than the spatial

104   resolution of the 3D image. Considering a voxel size of 1.75 μm of the 3D data set, and a minimum

105   extension of pores of two voxels in one direction, which can be separated by the algorithm, a minimum

106   pore size of 3.5 μm (or minimum pore radius of 1.75 μm) has to be regarded as effective resolution limit of

107   μ-CT. Therefore, the pore volume determined by μ-CT does not take into account the pore space with radii

108   smaller than 1.75 μm. For this study, a nanotom S 180 X-ray μ-CT equipment (GE sensing and inspection

109   technologies) has been used. For pore network separation, a combination of manual thresholding and

110   watershed algorithms has been applied to achieve the qualitatively best separated pore space. Additionally,

111   separation results have been cross checked with the images of scanning electrode microscopy (SEM). More

112   details on the digital image analysis workflow can be found in Halisch et al. (2016). The digital image

113   analysis of the 3-D μ-CT data sets provide for each individual pore the volume and the pore radius of the

114   largest sphere that can be placed inside this pore (maximum inscribed sphere method). The resulting

115   equivalent pore radius is referred to as pore body radius r_b. Adding up the pore volumes starting with the

116   lowest pore radius yields the cumulative volume fraction of pores V_c (Eq. (1)) as a function of the pore

117   body radius r_b.

118
119   From MIP, the entry sizes of pores and cavities, which is referred to as pore throat radius r_t, can be

120   determined according to the Washburn-equation (Washburn, 1921)

121          $$r_t = -\frac{2 \cdot \gamma \cdot \cos\theta}{P_c},$$ (2)

122   with γ = 0.48 N/m being the surface tension of mercury, θ = 140° the contact angle between mercury and

123   the solid minerals, and P_c the pressure of the liquid mercury that is referred to as capillary pressure. The

124   MIP experiments have been conducted with the PASCAL 140/440 instrument from Thermo Fisher

125   (Mancuso et al., 2012), which covers a pressure range between 0.015 MPa and 400 MPa corresponding to a

126   pore throat radius range from (at best) 1.8 nm to 55 μm. The samples have been evacuated before the MIP

127   experiment. Starting with low pressure, the pores with larger pore throats are filled with mercury. While

128   increasing the pressure, the pores with smaller throats are filled. Reaching a certain pressure level P_c, a

129   cumulative volume of mercury (V_{Hg}) has intruded into the sample that corresponds to the pore volume

130   being accessible by pore throats radii larger or equal r_t according to Eq. (2). The volume V_{Hg} corresponds to

131   the pore volume $V(>r_t)$. It should be noted that the volume of larger pores, which are shielded by narrower

132   throats, is attributed to the pore throat radius (e.g. Kruschwitz et al., 2016). Knowing the total pore volume

133   V_p, the saturation of the sample with mercury S_{Hg} can be determined. A conventional capillary pressure

134   curve displays the relationship between the saturation of the sample with mercury S_{Hg} as a function of

135   capillary pressure P_c (e.g. Thomeer, 1960). Using the following simple transformations

$$S_{Hg} = \frac{V_{Hg}}{V_p} = \frac{V(>r_t)}{V_p} = \frac{V_p - V(<r_t)}{V_p} = 1 - V_c \,, \tag{3}$$

137   the cumulative volume fraction of pores V_c as defined in Eq. (1) can be determined as a function of r_t.

138
139   The NMR relaxometry experiment provides the distribution of the transversal relaxation time $b(T_2)$. The

140   individual relaxation time T_2 is attributed to a pore space with a certain surface to volume ratio A/V by

$$\frac{1}{T_2} = \rho\left(\frac{A}{V}\right), \tag{4}$$

142   with ρ being the surface relaxivity. Considering that for a capillary tube model with cylindrical pores of

143   uniform radius r, the surface to volume ratio equals $2/r$, we get the following linear relationship between

144   pore radius r and relaxation time T_2 (e.g. Kleinberg, 1996):

$$r = 2\rho T_2 \,. \tag{5}$$

146   The NMR experiments have been performed with a Magritek Rock Core Analyzer equipment operating at a

147   Larmor frequency of 2 MHz at room temperature (~ 20°C) and ambient pressure. After drying at 105°C for

148   more than 24 hours in vacuum, the samples have been fully saturated with tap water with a conductivity of

149   about 25 mS/m. NMR measurements can be calibrated to get the porosity of the sample. The early time

150   decay signal corresponds to the total water content. The range of resolved pore radii depends on the used

151   value of surface relaxivity. The amplitude b attributed to an individual relaxation time T_2 is related to the

152   volume fraction of pores with the respective pore radius. Considering the larger pores, the resulting radius

153   corresponds to r_b. The smaller pore throats with lower volume yield a lower signal at shorter relaxation

154   times. The cumulative volume fraction of pores V_c is determined by adding up the individual b values

155   starting from the smallest relaxation time and normalizing to the total sum of all b values.

156
157   Another approach to derive a pore size distribution is based on the SIP method (Revil et al., 2014, Zhang et

158   al., 2017). We use the Debye decomposition (Nordsiek and Weller, 2008) to determine the electrical

159   relaxation time distribution as well as the total chargeability from complex conductivity spectra. To

160   transform the relaxation time distribution into a pore size distribution, we adopt the approach proposed by

161   Schwarz (1962) and applied by Revil et al. (2012) for the Stern layer polarization model:

$$r = \sqrt{2\tau D_{(+)}} \,, \tag{6}$$

163   with $D_{(+)}$ being the diffusion coefficient of the counter-ions in the Stern layer and τ being the relaxation

164   time. Originally, this equation describes the relation between the radius of spherical particles in an

165   electrolyte solution and the resulting relaxation time. Though it remains discussible whether the radius of

166   spherical grains can be simply replaced by the pore radius (Weller et al., 2016), we generally follow this

167   approach. Additionally, we assume a constant diffusion coefficient $D_{(+)} = 3.8 \times 10^{-12}$ m²/s as proposed by

168   Revil (2013).

169   The signal amplitude at a given relaxation time corresponds to the pore volume related to the pore radius

170   determined by Eq. (6). Considering the experience that the polarization is related to the specific surface

171   area per unit pore volume (e.g. Weller et al., 2010), we assume that the IP signals are caused by the ion-

172   selected active zones in the narrow pores that are comparable with the pore throats. Their size is quantified

173   by the pore throat radius r_t. Following the procedure proposed by Zhang et al. (2017), the cumulative

174   volume fraction V_c corresponds to the ratio of cumulative chargeability to total chargeability. Considering

175   the restricted range of pore radii resolved by SIP, a correction of the maximum V_c becomes necessary.

176   Complex conductivity spectra were recorded using a four-electrode sample holder as described by Schleifer

177   et al. (2002). The spectra were acquired with the impedance spectrometer ZEL-SIP04 (Zimmerman et al.,

178   2008) in a frequency range between 0.002 Hz and 45 kHz at a constant temperature of about 20 °C.

179   Considering that the complex conductivity spectra are affected by electromagnetic coupling effects or other

180   polarization effects at higher frequencies and by a lower signal to noise ratio for lower frequencies, we

181   focus on the frequency range between 0.01 Hz and 100 Hz. The samples were fully saturated with a

182   sodium-chloride solution with a conductivity of 100 mS/m. At least two measurements were performed for

183   each sample to verify the repeatability. The SIP method solely resolves a range of pore radii that depends

184   on the diffusion coefficient. Hence, using $D_{(+)} = 3.8 \times 10^{-12}$ m²/s in Eq. (6), we get a range of pore radii

185   between 0.1 μm and 10 μm.

186

187   The procedures described above result in an individual curve displaying the logarithm of V_c versus the

188   logarithm of the pore radius for each method. Previous studies have compared the resulting curves (e.g.

189   Zhang and Weller, 2014; Zhang et al., 2017; Ding et al., 2017). The slope of the curves was used to get a

190   fractal dimension. It became obvious that the distribution curves indicate remarkable differences that are

191   caused by the physical principles of the used methods. The methods differ with regard to their limits of

192   resolution. The effective resolution of μ-CT is limited by the voxel size. Larger pores can be easily detected.

193   The MIP yields the widest range of pore radii. The pore radius is directly related to the pressure. A

194   similarly wide range of pore radii can be resolved by NMR. However, the transformation of the NMR

195   transversal relaxation time into a pore radius requires the surface relaxivity as scaling factor. In a similar

196   way, the transformation of the electrical relaxation time resulting from SIP into a pore radius is based on a

197   scaling factor that depends on the diffusion coefficient. Only a restricted range of pore radii can be resolved

198   by SIP.

199   Beside the range of pore radii, the geometrical extend of the pore radius differ among the methods. µ-CT

200   enables a geometrical description of the individual pore space considering the shape of the pore. The pore

201   radius can be determined in different ways. We use the average pore radius as an equivalent for the pore

202   body radius r_b. MIP is sensitive to the pore throat radius r_t that enables the access to larger pores behind the

203   throat. The NMR relaxation time is related the pore body radius r_b. We assume that the IP signals are

204   caused by the ion-selected active zones in the narrow pores that are comparable with the pore throats.

205   Regarding the differences of the methods, we present an approach that combines the curves to get more

206   information on the pore space geometry. Considering the two kinds of pore radii r_b and r_t, we use first µ-

207   CT and NMR to generate a combined curve displaying V_c as a function of r_b. In the next step, we link the

208   curves resulting from MIP and SIP to get a curve showing V_c as a function of the pore throat radius r_t.

209   It is fundamental that the total pore volume (or total porosity) has to be known. The cumulative pore

210   volume fraction should only consider the pore volume that is resolved in the regarded range of pore radii.

211   Considering the resolution of µ-CT, only the pore space with radii larger than the voxel size is determined.

212   The cumulative pore volume fraction at the limit of resolution has to be adjusted to the non-resolved pore

213   volume. In this way, the µ-CT curve gets a fixed position in the $V_c – r$ plot. Regarding NMR, the relaxation

214   time T_2 has to be transformed into a pore radius according to Eq. (5). The application of Eq. (5) requires the

215   knowledge of the surface relaxivity ρ, which is the necessary scaling factor that causes a shift of the V_c - r

216   curve along the axis of pore radius. Since NMR method is sensitive to the pore body radius, we expect a

217   similar V_c - r curve for NMR and µ-CT in the overlapping range of pore radii. The NMR curve is shifted

218   along the axis of pore radii until a good agreement between the two curves is reached. This procedure

219   enables the adjustment of the surface relaxivity.

220   MIP is used to generate the curve displaying V_c as a function of r_t over a wide range of pore radii. The SIP

221   curve is fixed at the MIP curve considering the coincidence at the largest pore radius resolved by SIP.

222   The two curves representing V_c as a function of both r_b and r_t are displayed in a double logarithmic plot.

223   The shift of the two graphs represents the ratio r_b/r_t. Additionally, the slope of the curves is related to the

224   fractal dimension.

225   **3 Sample material**

226   For this study, two different sandstone samples have been used: first, a Bentheimer sandstone, sample

227   BH5-2. The Bentheimer sandstone formation is exposed in outcrops just east of the Dutch-German border

228   in the vicinity of Bad Bentheim, Germany. The shallow-marine Bentheimer sandstone was deposited

229   during the Early Cretaceous (roughly 140 million years ago) and forms an important reservoir rock for

230   petroleum (Dubelaar et al., 2015). This sandstone is widely used for systematic core analysis due its simple

231 mineralogy and the quite homogeneous and well-connected pore space. It is mainly composed out of quartz,

232 contains some feldspar and about 5 vol.-% of kaolinite, which is a direct alteration product of the

233 potassium-bearing feldspar minerals. Accordingly, surface area as well as surface relaxivity values are

234 mostly controlled by the kaolinite for this rock. Figure 1 (A and B)gives 2-D impressions of the pore

235 system of the Bentheimer sandstone sample. The pore space in general is very well connected, featuring

236 many large and open pores (Fig.1, A & B, blue arrows) and can be described as a classical pore body –

237 pore throat – pore body system. Small pores are mostly found within the clayey agglomerations, which act

238 as (macro) pore filling material (Fig.1, A & B, red arrows) and which are homogeneously distributed

239 throughout the sample material. This favorable structure is directly reflected by the petrophysical properties

240 of this sandstone. The sample investigated in our study is characterized by a porosity of 0.238, a gas-

241 permeability of 425 mD and a specific surface area of 0.3 m²/g.

242 Secondly, a Röttbacher sandstone, sample RÖ10B, has been used. The Röttbacher sandstone is a fine-

243 grained, more muscovite-illite containing, and rather homogeneous material that was deposited during the

244 Lower Triassic era (roughly 250 million years ago). It is suitable for solid stonework and has been widely

245 used as building material for facades as well as for indoor and outdoor flooring. The Röttbacher sandstone

246 was included in a study on the relationship of pore throat sizes and SIP relaxation times reported by

247 Kruschwitz et al. (2016). This sandstone consists mostly of quartz, but features a higher amount of clay

248 minerals than the Bentheimer sample. Additionally, Fe-bearing minerals (e.g. haematite) have been formed

249 during its arid depository environment, giving this sandstone a distinct reddish color. Accordingly, surface

250 area as well as surface relaxivity are dominated by the clay and the Fe-bearing minerals and should be

251 significantly different than for the BH5-2 sample. Figure 1 (C and D) showcases an impression of the pore

252 space from 2-D imaging techniques. Though the (large) pore space is similar structured as it is for the

253 Bentheimer (pore body-throat-body system, Fig. 1, C & D, blue arrows), it is generally reduced (cemented)

254 by clay minerals and features a significantly higher amount of small pores within (Fig. 1, C & D, red

255 arrows). Accordingly, pore space related petrophysical properties classify a more compact rock. The

256 sample used for this study features a porosity of 0.166, which is lower than for the Bentheimer sandstone.

257 The gas-permeability is 34.5 mD, which is less than 10 % of the value determined for the Bentheimer

258 sandstone. The specific surface area has been measured with 1.98 m²/g and is hence nearly seven times

259 larger than for sample BH5-2, clearly underlining the impact of the clay content. The petrophysical

260 parameters for both samples are compiled in Table 1, whereas results from X-ray fluorescence analysis are

261 summarized in Table 2, regarding the most important mineral components of both sandstones that have

262 been used for this study.

263   **4 Results**

264   **4.1 Bentheimer sandstone**

265   We applied the methods μ-CT, MIP, NMR, and SIP to get insight into the pore radius distribution of the

266   Bentheimer sandstone sample BH5-2. Figure 2 displays the resolved porosity ϕ_r as a function of pore radius

267   for μ-CT and MIP data. The cumulative pore volume while progressing from larger to smaller pores $V(>r)$

268   is normalized to the total volume of the sample V_s and results in the resolved porosity

269    $$\phi_r = \frac{V(>r)}{V_s} ,$$ (7)

270   which reaches the true porosity ϕ as threshold value for r approaching zero.

271   As shown in Figure 2, the μ-CT method identifies the largest pores with pore body radii of about 100 μm.

272   The resolved porosity ϕ_r reaches a value of 0.184 at the limit of resolution of the μ-CT method (r_b=1.75

273   μm). The nearly horizontal curve progression for $r < 17$ μm indicates that no pores with radii lower than 17

274   μm were detected by μ-CT.

275   The MIP identifies the largest pore throats with a radius of about 30 μm. Reaching the limit of resolution of

276   the MIP, the resolved porosity approaches asymptotically the threshold value of 0.238. Though both

277   methods μ-CT and MIP yield the pore radius without any adjustable scaling factor, we observe differences

278   between the two curves $\phi_r(r)$ in Figure 2.

279   Applying the transformation in Eq. (3) for the MIP data and assuming a true porosity of 0.238, the

280   cumulative volume fraction of pores V_c can be displayed as a function of pore radius as shown in Figure 3.

281   The MIP curve gets a fixed position in the plot of Figure 3 without the need for any scaling. It covers a

282   wide range of pore radii.

283   The curves resulting from other methods have to be adjusted considering the limits of the range of pore

284   radii. The maximum of the μ-CT curve corresponds to $V_c = 1$ because no larger pore size has been detected

285   by other methods. The maximum resolved porosity of the sample as detected by MIP reaches 0.238. The

286   porosity determined by μ-CT reaches only 0.184 (Figure 2). This value corresponds to a fraction of 0.773

287   of the porosity determined by MIP. Therefore, the minimum of the μ-CT curve at the pore radius of 17 μm

288   has to be adjusted at $V_c = 1 - 0.773 = 0.227$, because this fraction of pore volume is related to pore radii

289   smaller than 17 μm. The shift of the μ-CT curve to larger pore radii in comparison with MIP is observed in

290   this plot, too.

291   The T_2 relaxation time distribution of sample BH5-2 is plotted in Figure 4. It indicates a distinct maximum

292   at a relaxation time of 330 ms and two weaker maxima at lower relaxation times. The T_2 relaxation time

293   distribution is transformed into a curve showing the cumulative intensity as a function of T_2. The total

294   intensity is attributed to the total pore volume. The volume fraction V_c corresponds to the ratio of

295   cumulative intensity to total intensity. In order to get the curve V_c as a function of pore radius, the

296   relaxation time T_2 has to be transformed into a pore radius using the surface relaxivity ρ as scaling factor in

297   Eq. (5). Since both µ-CT and NMR method are sensitive to the pore body radius, we expect a similar V_c - r

298   - curve in the overlapping range of pore radii. Assuming a coincidence of the two curves at V_c = 0.5, the

299   surface relaxivity is adjusted at ρ = 54 µm/s.

300   Considering the frequency range between 0.01 and 100 Hz and $D_{(+)}$ = 3.8×10^{-12} m²/s, the relaxation time

301   distribution derived from SIP is attributed to a restricted range of pore radii between 0.1 µm and 10 µm.

302   Assuming that the polarization signals originate from the pore throats, a similarity of pores size

303   distributions resulting from MIP and SIP can be expected. It should be noted that MIP provides the

304   distribution for a wider range of pore radii. Therefore, we adjust the value of V_c at the maximum radius of

305   the SIP to the corresponding value for the MIP curve.

4.2 Röttbacher sandstone

307   The Röttbacher sample was scanned with resolution 1.5 µm by µ-CT. As shown in Figure 6, the µ-CT

308   method identifies the largest pores with pore body radii of about 90 µm. The resolved porosity ϕ_r reaches a

309   value of 0.106 at the limit of resolution of the µ-CT method (r_b=1.5 µm). The nearly horizontal curve

310   progression for r < 10 µm indicates that no pores with radii lower than 10 µm were detected by µ-CT.

311   The MIP identifies the largest pore throats with a radius of about 50 µm. Reaching the limit of resolution of

312   MIP, the resolved porosity gets the value of 0.166. Applying the transformation in Eq. (3) on the MIP data

313   and assuming a true porosity of 0.166, the cumulative volume fraction of pores V_c is displayed as a function

314   of pore radius as shown in Figure 7.

315   We suppose that the MIP method detects the whole pore volume, a porosity of 0.106 recognized by µ-CT

316   corresponds to 63.9% of the total pore volume. Therefore, the minimum of the µ-CT curve at the pore

317   radius of 10 µm has to be adjusted at V_c = 1 – 0.639 = 0.361, because this fraction of pore volume is related

318   to pore radii smaller than 10 µm.

319   The T_2 relaxation time distribution of sample RÖ10B is plotted in Figure 4. It indicates a distinct maximum

320   at a relaxation time of 170 ms. Non-vanishing signals are observed at relaxation times below 0.1 ms. This is

321   an indication of the existence of very small pores in the Röttbacher sandstone.

322   The position of the NMR curve in the plot of Figure 7 depends on the surface relaxivity ρ. A coincidence

323   with the µ-CT curve at V_c = 0.5 requires a surface relaxivity of ρ = 237 µm/s for adjusting the NMR curve.

324   The complex conductivity spectra of the Röttbacher sample are displayed in Figure 5. The processing of the

325   spectra according to the described algorithm results in the V_c - r – curve as shown in Figure 7. The SIP

326   curve is fixed at the value V_c = 0.9 that has been determined by MIP for the maximum pore radius resolved

327   by SIP (r_t = 10 µm).

5 Discussion

The proposed approach in this study results in two pore size distribution curves for the two samples, which are in good accordance to the general pore space structures as described in section 3 and as visualized in Figure 1 (A to D). The first curve combines the distributions resulting from µ-CT and NMR. The µ-CT data provide a pore radius, which is regarded as pore body radius, without any scaling. The scaling of the NMR-curve provides an estimate of the surface relaxivity. The surface relaxivity of the Bentheimer sample reaches 54 µm/s, the corresponding value of the Röttbacher sample is with 237 µm/s much higher. The higher surface relaxivity in comparison with the Bentheimer sample is clearly justified considering the larger specific surface area (Table 1) and the significantly higher content of clay and iron-bearing minerals as indicated in Table 2 (e.g. Keating and Knight, 2010).

The two cumulative pore volume distribution curves for the Röttbacher sample (Figure 7) indicate over the wide range of pore radii a parallel progression with consistently higher values for the pore body radius (µ-CT and NMR) in comparison with the pore throat radius (MIP). The horizontal distance of the two curves yields the ratio r_b/r_t. Regarding the median pore radii at $V_c = 0.5$, a ratio $r_b/r_t = 9.13$ is determined. Considering smaller pores, a ratio $r_b/r_t = 12.15$ is indicated at $V_c = 0.05$.

The parallelism of the pore volume distribution curve is less developed for the Bentheimer sample (Figure 3). We observe a clear distance of the two curves in the range of larger pore radii. Regarding the median pore radii at $V_c = 0.5$, a ratio $r_b/r_t = 2.57$ is determined. For $V_c < 0.2$, the slope of the curves decreases and smaller distances between the curves are observed. The NMR curve in Figure 3 indicates for $V_c > 0.08$ larger pore radii in comparison with the MIP curve and confirms the relationship $r_b > r_t$. The reverse behavior in the interval $0.1 \ \mu m < r < 0.6 \ \mu m$ is possibly caused by the low volume fraction (3%) attributed to this range of pore radii. It can be expected that the small amount of water in the small pores causes only weak signals in the NMR relaxometry. Certainly, the resolution of all methods is limited in the range of pore radii that contains only a small volume of water.

Beside the distances between the curves the individual slopes are regarded. The slope (s) of the curve log (V_c) versus log (r) is related to the fractal dimension D of the pore volume ($D = 3 - s$) (Zhang and Weller, 2014). We observe a varying slope in the investigated range of pore radii for the Bentheimer sample. The only range of more or less constant slope, which extends from pore radius 0.1 µm to 10 µm, corresponds to a fractal dimension $D_{MIP} = 2.678$ for MIP, $D_{NMR} = 2.776$ for NMR, and $D_{SIP} = 2.618$ for SIP.

We observe a constant slope of the NMR curve for the Röttbacher sample (Figure 7) in the interval $0.01 \ \mu m < r_b < 100 \ \mu m$. A similar slope is observed for the MIP curve in the interval $0.01 \ \mu m < r_t < 10 \ \mu m$. Considering the overlapping pore throat radii range between 0.1 µm and 10 µm, a fractal dimension D with values of 2.640 for MIP, and 2.661 for NMR has been determined. The slightly higher slope of the SIP curve results in a lower value of fractal dimension ($D = 2.533$).

362   Our approach enables the integration of SIP in the determination of a pore throat size distribution.

363   Considering the limited frequency range, only a limited range of pore throat radii can be reflected. Using a

364   fixed diffusion coefficient $D_{(+)} = 3.8 \times 10^{-12}$ m²/s, a range of pore throat radii between 0.1 µm and 10 µm is

365   resolved. The SIP curve is linked to the MIP curve at $r = 10$ µm. The proposed procedure results in a fair

366   agreement between SIP and MIP curves in the overlapping range of pore throat radius for both the

367   Bentheimer and the Röttbacher sample. In comparison with MIP, a slight overestimation of V_c is observed

368   for larger pore throat radii and a underestimation for lower pore throat radii. Considering the two samples

369   of the presented study, the assumption of a constant diffusion coefficient seems to be justified. Regarding

370   the discussion on the most relevant parameter that controls the relaxation time, our assumption that the pore

371   throat radius is related to the relaxation time is supported by the results.

372   **6 Conclusions**

373   Pore radii distributions have been determined by different methods (µ-CT, MIP, NMR, and SIP) for two

374   sandstone samples. The curves presenting the cumulative distribution of pore volume V_c as a function of

375   pore size have proved to be a suitable tool for comparison. It becomes obvious that the distribution curves

376   indicate remarkable differences that are based on the physical principles of the used methods. The methods

377   differ with regard to their limits of resolution. The effective resolution of µ-CT is limited by the voxel size

378   (3.5 µm). Larger pores can be easily detected. The MIP yields the widest range of pore radii. The pore radii

379   are directly related to the pressure interval. A similar wide range of pore radii can be achieved by NMR.

380   However, the transformation of the NMR transversal relaxation time into a pore radius requires the surface

381   relaxivity as scaling factor. In a similar way, the transformation of the electrical relaxation time resulting

382   from SIP into a pore radius is based on a scaling factor that depends on the diffusion coefficient. Only a

383   restricted range of pore radii (0.1 µm to 10 µm) can be resolved by SIP.

384   Beside the range of pore radii, the geometrical extend of the pore radius differ among the methods. µ-CT

385   enables a geometrical description of the individual pore space considering the shape of the pore. The pore

386   radius can be determined in different ways. We use the average pore radius as an equivalent for the pore

387   body radius r_b. MIP is sensitive to the pore throat radius r_t that enables the access to larger pores behind the

388   throat. The NMR relaxation time is related to an average pore body radius r_b. We assume that the IP signals

389   are caused by the ion-selected active zones in the narrow pores that are comparable with the pore throats.

390   Considering the two kinds of pore radii r_b and r_t, we use µ-CT and NMR to generate a combined curve

391   displaying V_c as a function of r_b. A good agreement between the two curves is achieved if they coincide at

392    $V_c = 0.5$. This condition is used to determine the surface relaxivity, which is in good accordance to the

393   investigated surface area and mineralogy of the sample materials. MIP is used to generate the curve

394 displaying V_c as a function of r_t over a wide range of pore radii. The SIP curve is fixed at the MIP curve

395 considering the coincidence at the largest pore radius resulting from SIP.

396 The two curves representing V_c as a function of both r_b and r_t are displayed in a double logarithmic plot.

397 The shift of the two graphs represents the ratio r_b/r_t. Additionally, the slope of the curves is related to the

398 fractal dimension.

399 The investigations on the samples demonstrate that the porosity increases using a method with a higher

400 resolution. Both porosity and pore volume are parameters that depend on the resolution. The fractal

401 dimension describes the size of geometric objects as a function of resolution. Therefore, the knowledge on

402 fractal behavior enables upscaling and downscaling of geometric quantities. The Bentheimer sandstone

403 sample is characterized by a ratio $r_b/r_t = 2.57$ for the larger pores. A fractal behavior is observed in the

404 range of pore radii between 0.1 µm and 10 µm with an average $D = 2.69$ determined for the pore volume by

405 MIP, NMR, and SIP. The Röttbacher sandstone sample indicates with $r_b/r_t = 9.13$ a larger ratio between

406 pore body radius and pore throat in comparison with the Bentheimer sample. An average fractal dimension

407 of $D = 2.61$ is determined for the Röttbacher sample.

408 **Acknowledgements**

409 The authors thank Sven Nordsiek (University Bayreuth) for the Debye decomposition of the SIP data,

410 Dietmar Meinel (BAM, Berlin) for supporting the CT analysis, Carsten Prinz (BAM, Berlin) for providing

411 the MIP data, and Mike Müller-Petke as well as Raphael Dlugosch (both LIAG) for the acquisition of the

412 NMR spectra for this study. Dr. Zeyu Zhang thanks Bundesanstalt für Materialforschung und –prüfung

413 (BAM, Berlin) for the Adolf-Martens-Fellowship that enabled his stay in Germany for the experimental

414 research.

415 **References**

416 Avnir, D., and Jaroniec, M.: An isotherm equation for adsorption on fractal surfaces of heterogeneous

417 porous materials, Langmuir, 5, 6, 1412–1433, 1989.

418 Avnir, D., Farin, D., and Pfeifer, P.: Molecular fractal surfaces, Nature, 308, 261-263, 1984.

419 Daigle, H., and Johnson, A.: Combining Mercury Intrusion and Nuclear Magnetic Resonance

420 measurements using percolation theory, Transp Porous Med, 111, 669, doi: 10.1007/s11242-015-0619-1,

421 2016.

422   Ding, Y., Weller, A., Zhang, Z., and Kassab, M.: Fractal dimension of pore space in carbonate samples
423   from Tushka Area (Egypt), Arabian Journal of Geosciences, 10, 388, doi: 10.1007/s12517-017-3173-z,
424   2017.

425   Dubelaar, W. C., and Nijland, T. G.: The Bentheim Sandstone: geology, petrophysics, varieties and its use
426   as dimension stone, in: Engineering Geology for Society and Territory, 8, Lollino, G., Giordan, D.,
427   Marunteanu, C., Christaras, B., Yoshinori, I., and Margottini, C. (Eds.), Springer International Publishing,
428   Switzerland, 557-563, 2015.

429   Gaboreau, S., Robinet, J. C., Tournassat, C., and Savoye, S.: Diffuse transport in clay media: µm to nm
430   scale characterization of pore space and mineral spatial organization: International Meeting Clays in
431   Natural and Engineered Barriers for Radioactive Waste Confinement, Montpellier, France, October 2012,
432   hal-00705345, 2012.

433   Halisch, M., Schmitt, M., and Fernandes, C. P.: Pore Shapes and Pore Geometry of Reservoirs Rocks from
434   µ-CT Imaging and Digital Image Analysis, in: Proceedings of the Annual Symposium of the SCA 2016,
435   Snowmass, Colorado, USA, 21-26 August 2016, SCA2016-093, 2016.

436   Keating, K., and Knight, R.: A laboratory study of the effect of Fe(II)-bearing minerals on nuclear magnetic
437   resonance (NMR) relaxation measurements, Geophysics, 75 (3), F71–F82, 2010.

438   Keller, L. M., Holzer, L., Wepf, R., Gasser, P., Münch, B., and Marschall, P.: On the application of focused
439   ion beam nanotomography in characterizing the 3D pore space geometry of Opalinus clay, Physics and
440   Chemistry of the Earth, 36, 1539-1544, doi:10.1016/j.pce.2011.07.010, 2011.

441   Kelokaski, M., Siitari-Kauppi, M., Sardini, P., Mori, A., and Hellmuth, K.H.: Characterisation of pore
442   space geometry by ^{14}C-PMMA impregnation-development work for in situ studies, Journal of Geochemical
443   Exploration,   90, 45-52, doi:10.1016/j.gexplo.2005.09.005, 2005.

444   Kleinberg, R. L.: Utility of NMR T_2 distributions, connection with capillary pressure, clay effect, and
445   determination of the surface relaxivity parameter ρ2, Magnetic Resonance Imaging, 14, 761–767, 1996.

446   Kruschwitz, S., Prinz C., and Zimathies A.: Study into the correlation of dominant pore throat size and SIP
447   relaxation frequency, Journal of Applied Geophysics, 135, 375-386, 2016.

448   Mandelbrot, B. B.: Fractals: form, chance, and dimension, Freeman, San Francisco, 1977.

449   Mandelbrot, B. B.: Fractal geometry of nature, Freeman, San Francisco, 1983.

450 Mancuso, C., Jommi, C., and D'Onza, F. (Eds.): Unsaturated Soils: Research and Applications, Volume 1,
451 Springer-Verlag Berlin Heidelberg, 123-130, doi: 10.1007/978-3-642-31116-1, ISBN: 978-3-642-31115-4
452 (Print), 2012.

453 Meyer, K., Klobes, P., and Röhl-Kuhn, B.: Certification of reference material with special emphasis on
454 porous solids, Crystal Research and Technol., 32, 173-183, 1997.

455 Mesquita, P., Souza, A., Carneiro, G., Boyd, A., Ferreira, F., Machado, P., and Anand, V.: Surface
456 relaxivity estimation and NMR-MICP matching in diffusion coupled rocks, in: Proceedings of the Annual
457 Symposium of the SCA 2016, Snowmass, Colorado, USA, 21-26 August 2016, SCA2016-059, 2016.

458 Nordsiek, S., and Weller, A.: A new approach to fitting induced-polarization spectra, Geophysics, 73, 6,
459 F235-F245, doi: 10.1190/1.2987412, 2008.

460 Pape, H., Riepe, L., and Schopper, J. R.: A pigeon-hole model for relating permeability to specific surface,
461 The Log Analyst, 23, No. 1, 5–13, 1982.

462 Peth, S., Horn, R., Beckmann, F., Donath, T., Fischer, J., and Smucker, A. J. M.: Three-dimensional
463 quantifi cation of intra-aggregate pore-space features using Synchrotron-Radiation-Based
464 Microtomography, Soil Science Society of America journal, 72, 4, 897-907, doi: 10.2136/sssaj2007.0130,
465 2008.

466 Revil, A., Koch, K., and Holliger, K.: Is it the grain size or the characteristic pore size that controls the
467 induced polarization relaxation time of clean sands and sandstones?, Water Resources Research, 48,
468 W05602, doi: 10.1029/2011WR011561, 2012.

469 Revil, A.: Effective conductivity and permittivity of unsaturated porous materials in the frequency range 1
470 mHz-1GHz, Water Resources Research, 49, 306-327, doi: 10.1029/2012WR012700, 2013.

471 Revil, A., Florsch, N., and Camerlynck, C.: Spectral induced polarization porosimetry, Geophysical Journal
472 International, 198, 1016-1033, doi: 10.1093/gji/ggu180, 2014.

473 Rouquerol, J., Avnir, D., Fairbridge, D. C. W., Everett, D. H., Haynes, J. H., Pernicone, N., Ramsay, J. D.
474 F., and Sing, K. S. W., and Unger, K. K.: Recommendations for the characterization of porous solids (Technical
475 Report), Pure and Appl. Chem., 66, 1739-1758, 1994.

476 Schleifer, N., Weller, A., Schneider, S., and Junge, A.: Investigation of a Bronze Age plankway by spectral
477 induced polarization, Archeological Prospection, 9, 243–253, doi: 10.1002/arp.194, 2002.

478 Schwarz, G.: A theory of the low-frequency dielectric dispersion of colloidal particles in electrolyte
479 solution, Journal of Physical Chemistry, 66, 2636-2642, doi: 10.1021/j100818a067, 1962.

480 Thomeer, J. H. M.: Introduction of a pore geometrical factor defined by the capillary pressure curve,
481 Journal of Petroleum Technology, 12(3), 73-77, 1960.

482 Washburn, E. W.: The dynamics of capillary flow, Physical Review, 17, 3, 273-283, 1921.

483 Weller, A., Nordsiek, S., and Debschütz, W.: Estimating permeability of sandstone samples by nuclear
484 magnetic resonance and spectral-induced polarization, Geophysics, 75, E215 – E226, doi:
485 10.1190/1.3507304, 2010.

486 Weller, A., Zhang, Z., Slater, L., Kruschwitz, S., and Halisch, M.: Induced polarization and pore radius – a
487 discussion, Geophysics, 81, 5, D519-526, doi:10.1190/GEO2016-0135.1, 2016.

488 Zhang, Z., and Weller, A.: Fractal dimension of pore space geometry of an Eocene sandstone formation,
489 Geophysics, 79, D377-387, doi:10.1190/GEO2014-0143.1, 2014.

490 Zhang, Z., Weller, A., and Kruschwitz, S.: Pore radius distribution and fractal dimension derived from
491 spectral induced polarization, Near Surface Geophysics, 15, 625-632, doi: 10.3997/1873-0604.2017035,
492 2017.

493 Zimmermann, E., Kemna, A., Berwix, J., Glaas, W., and Vereecken., H.: EIT measurement system with
494 high phase accuracy for the imaging of spectral induced polarization properties of soils and sediments,
495 Measurement Science and Technology, 19, 9, 094010, doi: 10.1088/0957-0233/19/9/094010, 2008.

496

497

498

499

500

501

502

Table 1: Petrophysical properties of the samples: porosity ϕ, permeability K, specific surface area S_m, formation factor F, dominant pore radius r_{dom}, effective pore radius r_{eff}, fractal dimensions determined from mercury intrusion porosimetry D_{MIP}, nuclear magnetic resonance D_{NMR}, and spectral induced polarization D_{SIP}, the surface relaxivity ρ, and the Diffusion coefficient $D_{(+)}$.

	unit	BH5-2	RÖ10B
Porosity (Triple weighing)		0.238	0.159
Porosity (μ-CT)		0.184	0.106
Porosity (MIP)		0.238	0.166
Permeability K	mD	425	34.5
Specific surface area	m²/g	0.30	1.98
Formation factor F		14.3	11.3
r_{dom} (MIP)	μm	11.4	4.9
$r_{eff} = (8FK)^{0.5}$	μm	6.97	1.77
D_{MIP}		2.678	2.640
D_{NMR}		2.776	2.661
D_{SIP}		2.618	2.533
Surface relaxivity ρ	μm/s	54	237
Diffusion coefficient $D_{(+)}$	m²/s	3.8×10^{-12}	3.8×10^{-12}

Table 2: Mineral components of the samples from X-ray Fluorescence analysis.

	Selected Mineral Phases from X-Ray Fluorescence [weight-%]						
Sample	SiO_2	TiO_2	Al_2O_3	Fe_2O_3	CaO	Na_2O	K_2O
BH5-2	97.84	0.048	1.2	0.05	0.019	0.02	0.355
RÖ10B	87.06	0.356	6.06	1.07	0.225	0.13	3 679
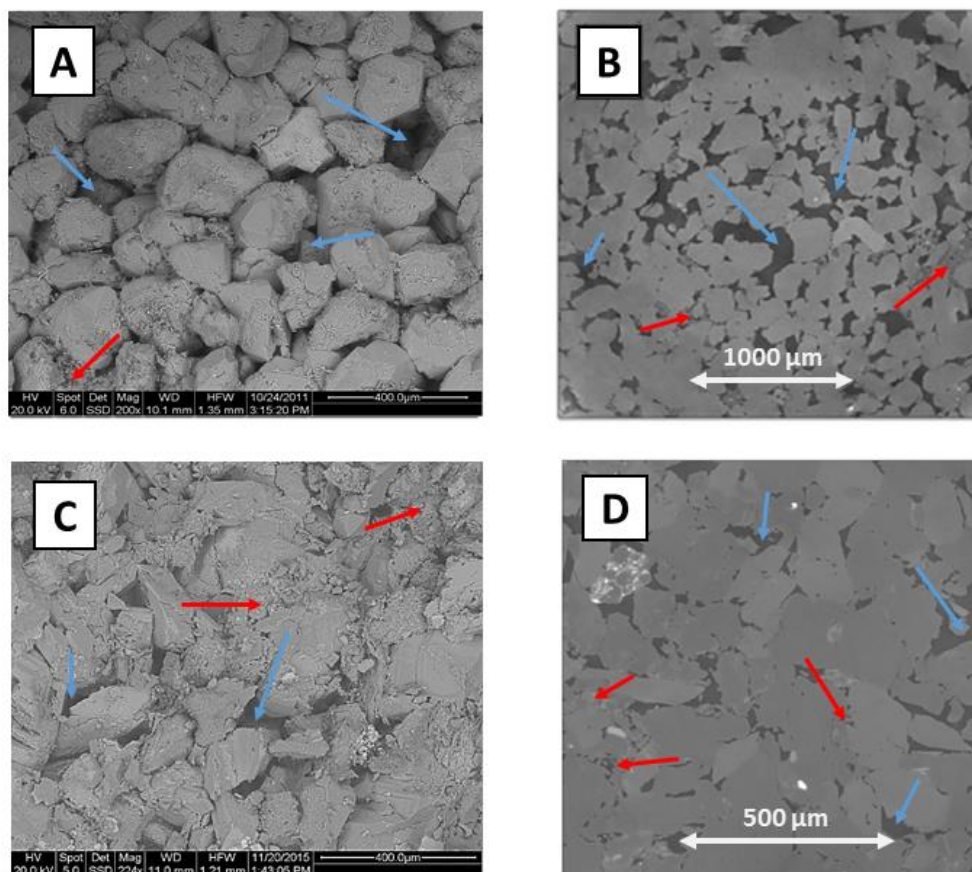
Figure 1: SEM (A) and 2D (B) CT views upon the minerals and pore structure of the investigated sample of Bentheimer sandstone, and SEM (C) and 2D (D) CT views upon the minerals and pore structure of the investigated sample of Röttbacher sandstone. Blue arrows indicate open pore spaces, red arrows indicate clay agglomerations and pore fillings.
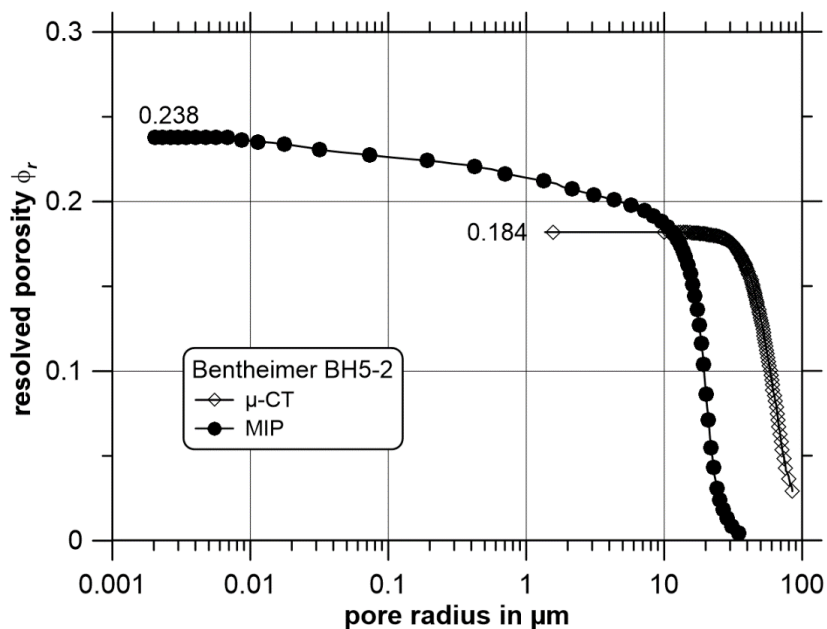
519
520 **Figure 2: The recognized porosity and pore size range of Bentheimer sandstone sample BH5-2.**
521
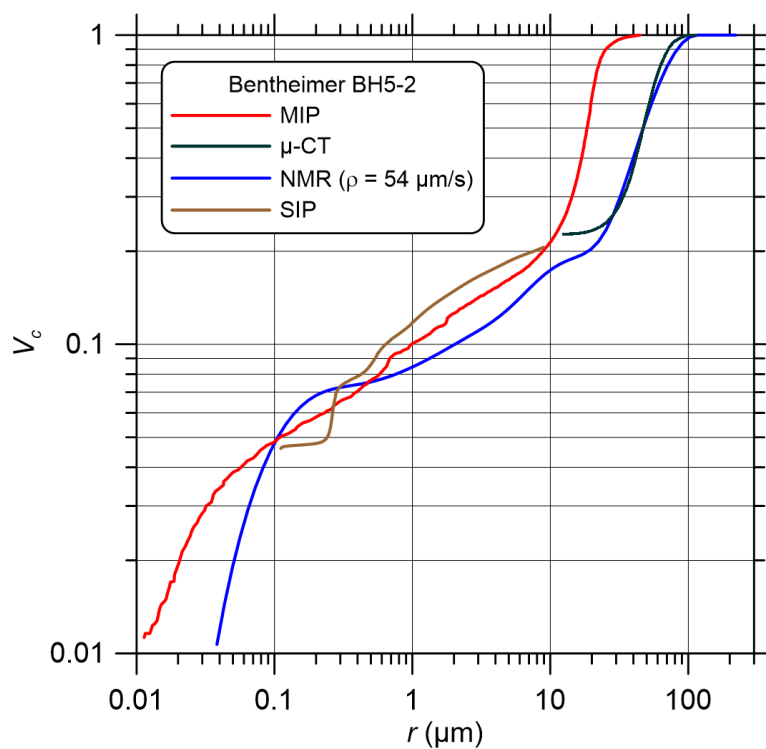
522
523 **Figure 3: The comparison of V_c-r curves determined from MIP, μ-CT, NMR and SIP for Bentheimer sandstone**
524 **sample BH5-2.**
525
526
527
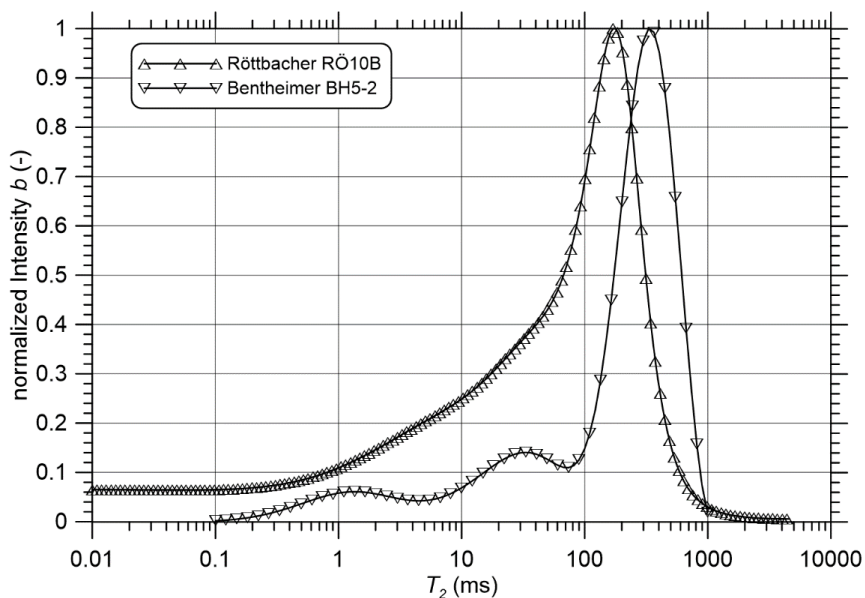
528
529 **Figure 4: The NMR T_2 relaxation time distributions of samples BH5-2 and RÖ10B.**

530
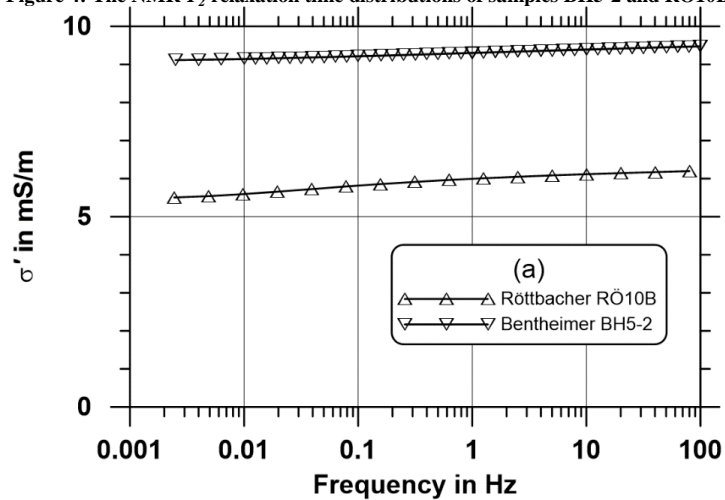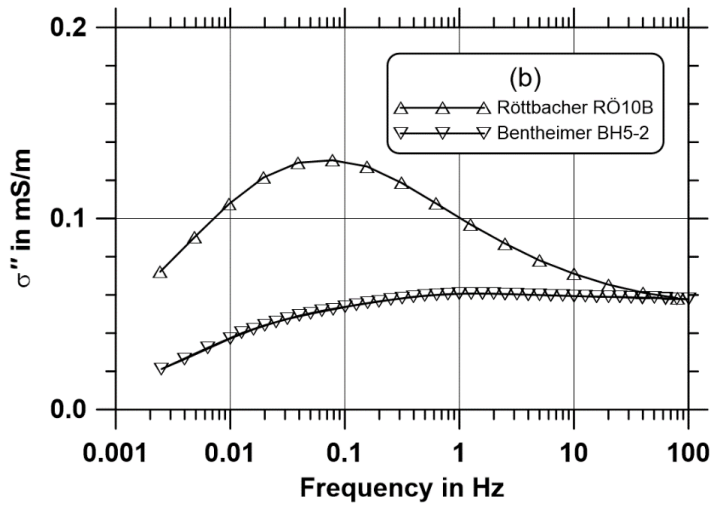
531
532
533
534 **Figure 5: Measured complex conductivity spectra of samples BH5-2 and RÖ10B. a) real part of conductivity, b)**
535 **imaginary part of conductivity.**
536
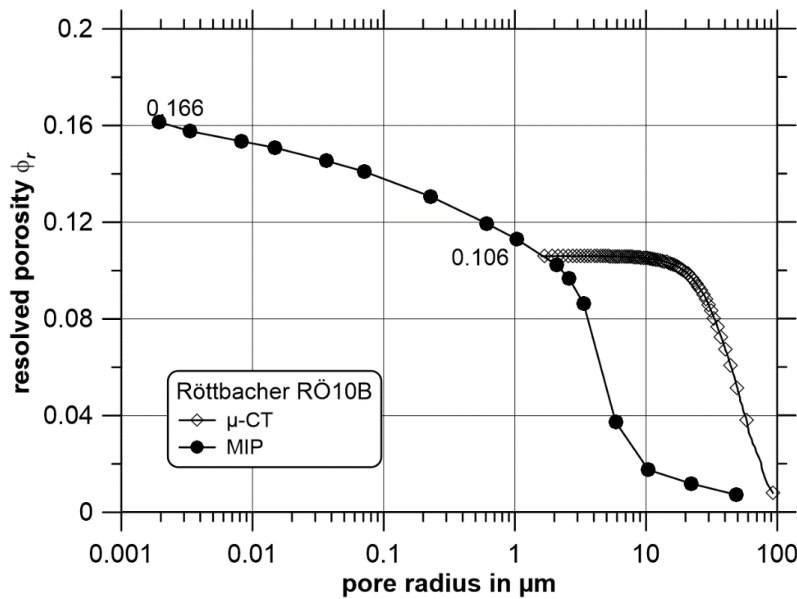
537
538 **Figure 6: The recognized porosity and pore size range of Röttbacher sandstone sample RÖ10B.**
539
540
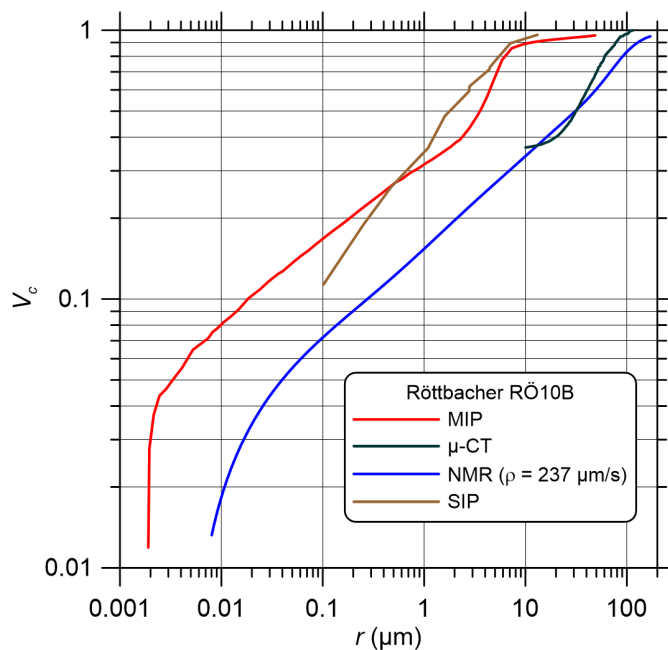
Figure 7: The comparison of V_c-r curves determined from MIP, μ-CT, NMR and SIP for Röttbacher sandstone sample RÖ10B.